Article

Mitoenergetic Dysfunction Triggers a Rapid Compensatory Increase in Steady-State Glucose Flux

Dania C. Liemburg-Apers,[1,3,4] Tom J. J. Schirris,[2,3] Frans G. M. Russel,[2,3] Peter H. G. M. Willems,[1,3,4] and Werner J. H. Koopman[1,3,4,*]

[1]Department of Biochemistry and [2]Department of Pharmacology and Toxicology, Radboud Institute for Molecular Life Sciences, Radboud University Medical Center, Nijmegen, The Netherlands; [3]Centre for Systems Biology and Bioenergetics, Radboud University and Radboud University Medical Center, Nijmegen, The Netherlands; and [4]Nijmegen Center for Mitochondrial Disorders, Radboud University Medical Center, Nijmegen, The Netherlands

ABSTRACT ATP can be produced in the cytosol by glycolytic conversion of glucose (GLC) into pyruvate. The latter can be metabolized into lactate, which is released by the cell, or taken up by mitochondria to fuel ATP production by the tricarboxylic acid cycle and oxidative phosphorylation (OXPHOS) system. Altering the balance between glycolytic and mitochondrial ATP generation is crucial for cell survival during mitoenergetic dysfunction, which is observed in a large variety of human disorders including cancer. To gain insight into the kinetic properties of this adaptive mechanism we determined here how acute (30 min) inhibition of OXPHOS affected cytosolic GLC homeostasis. GLC dynamics were analyzed in single living C2C12 myoblasts expressing the fluorescent biosensor FLII^{12}Pglu-700$\mu\delta$6 (FLII). Following in situ FLII calibration, the kinetic properties of GLC uptake (V_1) and GLC consumption (V_2) were determined independently and used to construct a minimal mathematical model of cytosolic GLC dynamics. After validating the model, it was applied to quantitatively predict V_1 and V_2 at steady-state (i.e., when $V_1 = V_2 = V_{steady\text{-}state}$) in the absence and presence of OXPHOS inhibitors. Integrating model predictions with experimental data on lactate production, cell volume, and O_2 consumption revealed that glycolysis and mitochondria equally contribute to cellular ATP production in control myoblasts. Inhibition of OXPHOS induced a twofold increase in $V_{steady\text{-}state}$ and glycolytic ATP production flux. Both in the absence and presence of OXPHOS inhibitors, GLC was consumed at near maximal rates, meaning that GLC consumption is rate-limiting under steady-state conditions. Taken together, we demonstrate here that OXPHOS inhibition increases steady-state GLC uptake and consumption in C2C12 myoblasts. This activation fully compensates for the reduction in mitochondrial ATP production, thereby maintaining the balance between cellular ATP supply and demand.

INTRODUCTION

Glucose (GLC) is among the prime substrates for cellular energy production and serves as a precursor for various biomolecules such as glycoproteins and glycolipids. Hence, the capacity of a cell for GLC uptake and conversion greatly impacts on its energetic and functional state. GLC uptake is mediated by specific facilitative GLC transporters (Gluts). These integral plasma membrane (PM) proteins belong to the solute carrier 2A subfamily, which consists of 14 different members that differ in their substrate specificity, transport kinetics, tissue distribution, and mode of regulation. The rate of Glut-mediated cellular GLC uptake depends on the amount of active Gluts on the PM, their kinetic properties, and the magnitude of the trans-PM glucose gradient, which co-depends on the extracellular free GLC concentration ($[GLC]_{ext}$) and the cytosolic free GLC concentration ($[GLC]_c$). Once taken up, GLC is phosphorylated by the glycolysis enzyme hexokinase (HK) to form glucose-6-phosphate (G6P). Subsequently, G6P is converted into pyruvate (PYR) and imported into mitochondria to fuel the tricarboxylic acid (TCA) cycle. The latter produces NADH (reduced nicotinamide adenine dinucleotide) and $FADH_2$ (reduced flavin adenine nucleotide), which serve as substrates for the mitochondrial oxidative phosphorylation (OXPHOS) system. Alternatively, PYR can be reversibly converted into lactate (LAC) by lactate dehydrogenase that is released by the cell into the extracellular medium. The OXPHOS system consists of five multiprotein complexes (CI-CV) that generate ATP by chemiosmotic coupling (1). CI-CIV constitute the electron transport chain that extracts electrons from NADH (at CI) and $FADH_2$ (at CII). Subsequently, the electrons are transported to CIII and from thereon to CIV where they react with molecular oxygen (O_2). At CI, CIII and CIV protons (H^+) are transported from the mitochondrial matrix across the mitochondrial inner membrane to generate an inward-directed proton-motive force (PMF). Driven by the PMF, controlled H^+ back-flux via CV (i.e., the F_oF_1-ATP synthase) is used to synthesize ATP from ADP and inorganic phosphate (P_i). ATP is generated by GLC breakdown during glycolysis (2 ATP per GLC molecule), by the TCA cycle (2 ATP per GLC molecule) and by the OXPHOS system

Submitted April 10, 2015, and accepted for publication August 3, 2015.

*Correspondence: werner.koopman@radboudumc.nl

Editor: David Piston.

0006-3495/15/10/1372/15

http://dx.doi.org/10.1016/j.bpj.2015.08.002

(32 ATP per GLC molecule). The relative contribution of these systems to cellular ATP production depends on many parameters including the cell type and the nature/availability of energy substrates. In practice, the actual number of ATP molecules generated probably lies within the range of 29–30 ATP molecules per oxidized GLC molecule (2).

In case of mitochondrial dysfunction, increased extracellular LAC levels were observed in fibroblasts from patients with mitochondrial disease (3), mouse embryonic fibroblasts (MEFs) from *NDUFS4*$^{-/-}$ mice with isolated CI deficiency (4), skin fibroblasts from patients with myoclonic epilepsy with ragged red fibers syndrome (5), myotubes overexpressing the mitochondrial uncoupling protein 3 (6), polymerase gamma mutator mice (7), and human embryonic kidney 293 cells with a knockdown of the CI subunit NDUFS3 (8). In addition, drug-induced mitochondrial dysfunction stimulated GLC uptake in Clone 9 cells (9–13) and Glut1 upregulation and enhanced GLC uptake was shown in cancer cells (14,15). These results suggest that glycolysis-mediated ATP generation is activated by mitochondrial dysfunction (5). Currently, the balance and interactions between GLC uptake, glycolysis- and OXPHOS-mediated ATP production, as well as their regulation, is a subject of intense study (16–20). However, the various components of this dynamic system cannot be simultaneously accessed by experimental studies in single living cells. This necessitates the use of mathematical models (21–27).

In this study, we aimed to demonstrate how acute OXPHOS dysfunction affects steady-state GLC uptake and consumption, LAC production, O_2 consumption, and ATP production in C2C12 myoblasts. To this end we integrated experimental results with in silico predictions of a minimal model of GLC dynamics. This model correctly predicted the glycolytic flux in control and OXPHOS-inhibited cells and revealed that glycolysis and mitochondria equally contribute to ATP production when OXPHOS is active. We observed that acute OXPHOS inhibition twofold increases GLC uptake and consumption, thereby fully compensating for the loss in OXPHOS-mediated ATP generation and maintaining steady-state ATP homeostasis.

MATERIALS AND METHODS

Chemicals

Sodium iodoacetic acid (IAA), cytochalasin B (CytoB), cytochalasin D (CytoD), antimycin A (AA), and p-trifluoromethoxy carbonyl cyanide phenyl hydrazone were obtained from Sigma-Aldrich (Zwijndrecht, The Netherlands). Piericidin A (PA) was obtained from Enzo Life Sciences (Raamsdonksveer, The Netherlands).

Cell culture

C2C12 myoblasts were cultured at 37°C (95% air, 5% CO_2) in Dulbecco's modified eagle's medium (DMEM-32430; Life Technologies – Invitrogen, Bleiswijk, The Netherlands), supplemented with 10% (v/v) fetal bovine serum (FBS). C2C12 myoblasts were seeded in fluorodishes (#FD35-100, World Precision Instruments, Sarasota, FL) at a density of 40,000 cells/dish.

Transfection

1 day after seeding, C2C12 cells were at 40% confluence. 1 μg DNA was mixed with 6 μl lipofectamine (Invitrogen) in 0.5 ml FBS-free DMEM. Following 20 min incubation at room temperature the transfection mix was added to the cells in FBS-free DMEM. After 6 h this medium was replaced by DMEM containing 10% FBS. The glucose sensor FLII^{12}Pglu-700$\mu\delta$6 (FLII) (Addgene Plasmid #17866; (28)) and its high affinity variant FLIPglu-170nδ13V (Addgene Plasmid #18018; (29)) were a gift from Dr. Wolf Frommer (Department of Plant Biology, Carnegie Institution for Science, Stanford, CA).

Single cell microscopy of cytosolic GLC dynamics

At 24 h posttransfection the C2C12 myoblasts were at 80% confluence. Cells were washed and incubated for 3 min in HEPES/Tris (HT) buffer (adjusted to pH 7.4 with Tris) containing 4.2 mM KCl, 132 mM NaCl, 10 mM HEPES, 1.2 mM $MgCl_2$, and 1 mM $CaCl_2$. The HT buffer was then replaced with HT buffer containing 500 μM IAA and incubated for another 15 min. Subsequently the fluorodish was mounted onto an inverted microscope (30) (Axiovert 200M, Carl Zeiss BV, Sliedrecht, The Netherlands), equipped with a 40/1.3 NA Plan NeoFluar objective (Carl Zeiss) and a CoolSNAP HQ monochrome charge-coupled device (CCD)-camera (Roper Scientific, Vianen, The Netherlands). Microscopy hardware was controlled using Metafluor 6.0 software (Universal Imaging, Downingtown, PA). FLII and FLIPglu-170nδ13V were excited at 430 nm (CFP) for 300 ms using a Polychrome IV monochromator system (TILL Photonics, Gräfelfing, Germany). CFP fluorescence was detected using a 455DRLP dichroic mirror (XF2034, Omega Optical Inc, Brattleboro, VT) and a 480AF30 (XF3075; Omega) emission filter. Citrine emission ($Citrine_{FRET}$) was measured using 430 nm excitation light (during 200 ms) and emission was detected using the 455DRLP dichroic mirror and a 535AF26 emission filter (XF3079; Omega). Time-lapse recordings were performed using an acquisition interval of 2.5 s.

LAC measurements

C2C12 myoblasts were seeded in a T25 culture flask and cultured for 1 day, as described above. Cells were then incubated in 1 ml HT buffer containing 2 mM GLC and either vehicle or mitochondrial inhibitors for 60–90 min. The buffer was collected and centrifuged for 5 min at 600 $\times$ g. LAC levels were quantified using an Architect chemical analyzer (Abbott B.V., Hoofddorp, The Netherlands). For each sample, the cell number was determined using a Burker Turk hemocytometer.

O_2 consumption measurements

For respirometry analysis (31) C2C12 myoblasts were counted using a Scepter cell counter (Millipore, Billerica, MA) and 1.5 $\times$ 10^6 cells were transferred to the temperature-controlled (37°C) chamber of an Oxygraph-2k controlled by Datlab 5 recording (2 s time interval) and analysis software (32) (Oroboros Instruments, Innsbruck, Austria). To measure O_2 consumption, cells were either resuspended in HT buffer containing 2 mM GLC or culture medium. After adding the cells to the respiration chamber, the O_2 consumption trace was allowed to stabilize for 10 min until routine respiration could be measured in the coupled state of respiratory control. The complex V (CV) inhibitor oligomycin A (2.5 μM) was then added to determine the leak respiration. The maximal capacity of the

electron transport chain (ETS value) was determined by subsequent titration with the mitochondrial uncoupler p-trifluoromethoxy carbonyl cyanide phenyl hydrazone. Finally, minimal respiration (ROX value) was assessed after adding a maximal concentration of the complex I (CI) inhibitor rotenone (0.5 μM) and of the complex III (CIII) inhibitor antimycin A (AA; 0.5 μM). This ROX value was subtracted from the other respiratory rates to correct for nonmitochondrial respiration.

Cellular ATP level measurements

The total cellular ATP level was measured after 24 h using an ATP bioluminescence assay kit according to the manufacturer's protocol (CLS II; Roche Applied Science, Mannheim, Germany). Briefly, cells were harvested and counted using a Scepter cell counter (Millipore) after which cellular ATP was released by adding the cell suspension to a boiling Tris-EDTA buffer (100 mM Tris, 4 mM EDTA, pH 7.75) for 2 min. Part of this solution was diluted 1:1 (v/v) with luciferase reagent, followed by measurement of the bioluminescence signal. ATP concentrations were calculated using a standard curve, and divided by cell count to obtain ATP values.

Image processing, statistical analysis, and mathematical modeling

Microscopy images were stored in native Metafluor format (Universal Imaging, Bedford Hills, NY) and analyzed off-line using Image Pro Plus 6.1 software (Media Cybernetics, Rockville, MD). Individual images were background corrected for each wavelength by subtracting the average intensity in an extracellular region of interest (ROI). Next, cell-derived fluorescence signals were quantified using cytosolic circular ROIs. Average values are presented as mean $\pm$ SE. Curve fitting and statistical analysis was performed using Origin Pro 6.1 (OriginLab, Northampton, MA) and GraphPad Prism 5 (Graphpad Software, La Jolla, CA). Unless stated otherwise, statistical significance was assessed using an unpaired Student's *t*-test and expressed as $^{***}p < 0.001$, $^{**}p < 0.01$, and $^{*}p < 0.05$ relative to the indicated condition. Mathematical modeling was performed using MATLAB/Simulink 6.1 (The MathWorks, Natick, MA).

RESULTS

In situ calibration of the FLII GLC sensor in C2C12 myoblasts

In this study, we used the GLC biosensor FLII (28), which is based on the fluorescence resonance energy transfer (FRET) principle, to monitor dynamic changes in free cytosolic GLC concentration ($[GLC]_c$). FLII consists of a GLC binding domain sandwiched between CFP and the yellow fluorescent protein mutant Citrine. The GLC binding domain is derived from a periplasmic protein expressed in *Escherichia coli* (33). When GLC binds, the emission of Citrine upon CFP excitation ($Citrine_{FRET}$) increases. Simultaneously, the CFP emission upon CFP excitation (CFP) will decrease (Fig. 1 *A*). GLC unbinding will induce the reverse effect and the emission ratio ($Citrine_{FRET}$/CFP) can be used as a readout of $[GLC]_c$. Manipulation of $[GLC]_c$ by changing the extracellular [GLC] $[GLC]_{ext}$ (see next section for details) induced antiparallel changes in $Citrine_{FRET}$ and CFP in FLII-expressing C2C12 myoblasts (Fig. 1 *B*, *upper panel*). No alterations in cellular volume upon $[GLC]_{ext}$ manipulation were observed, as indicated by the lack of parallel changes in the individual CFP and $Citrine_{FRET}$ emission signals (Fig. 1 *B*, *upper panel*). Inspection of the $Citrine_{FRET}$/CFP signal revealed identical dynamic emission ratio in different subcellular ROIs (Fig. 1 *A*, *inset*) and the whole cell (Fig. 1 *B*, *lower panel*). For quantitative analysis and mathematical modeling of $[GLC]_c$ dynamics, calibration of the FLII emission ratio is required. Using a cell permeabilization strategy with β-Escin (a triterpenoid saponin) was not useful because it induced a shift in FLII signals (data not shown), as reported previously for C2C12 cells (34). Therefore the in situ calibration curve was generated by incubating FLII-expressing C2C12 myoblasts with different $[GLC]_{ext}$ concentrations in the presence of the GLC consumption inhibitor IAA (500 μM). IAA inhibits the glycolysis enzyme glyceraldehyde 3-phosphate dehydrogenase leading to G6P accumulation and allosteric HK inhibition (35). Following a 30 min incubation with various $[GLC]_{ext}$ and IAA, the FLII emission ratio was stable (Fig. 1 *C*). This shows that $[GLC]_{ext}$ and $[GLC]_c$ are fully equilibrated, allowing calibration of the FLII emission ratio (35). For each $[GLC]_{ext}$ the measured ($Citrine_{FRET}$/CFP) emission ratio was corrected for the emission ratio obtained in the absence of extracellular GLC ($Citrine_{FRET}$/$CFP_{0\ mMGLC}$). This corrected emission ratio was termed R_{corr}. The experimental in situ calibration curve was fitted using a Michaelis-Menten equation:

$$R_{corr} = \frac{R_{max} \times [GLC]_c}{K_m + [GLC]_c}, \quad (1)$$

with $[GLC]_c$ in mM, R_{corr} equaling the corrected FLII emission ratio (as defined above) and K_m representing the in situ FLII glucose affinity (in mM). Fitting yielded a maximal FLII emission ratio (R_{max}) of 3.6 $\pm$ 0.4 and a K_m of 1.9 $\pm$ 0.5 mM (Fig. 1 *D*). To allow calculation of $[GLC]_c(t)$ from the measured $R_{corr}(t)$, Eq.1 was rearranged into:

$$[GLC]_c(t) = \frac{K_m \times R_{corr}(t)}{R_{max} - R_{corr}(t)}. \quad (2)$$

Analysis of GLC uptake and consumption in C2C12 myoblasts

In the most simple case, (Fig. 2 *A*) dynamic changes in $[GLC]_c$ (i.e. $[GLC]_c(t)$) depend on the rate of GLC entry (V_1) across the PM and the rate of GLC consumption in the cell (V_2):

$$\frac{d[GLC]_c}{dt} = V_1 - V_2. \quad (3)$$

Cellular GLC entry is mediated by Gluts (36). Quantitative polymerase chain reaction (Q-PCR) analysis revealed that *Glut isoform 1* (37) is highly expressed in C2C12 myoblasts, whereas Glut2, Glut3, and Glut4 were not detected

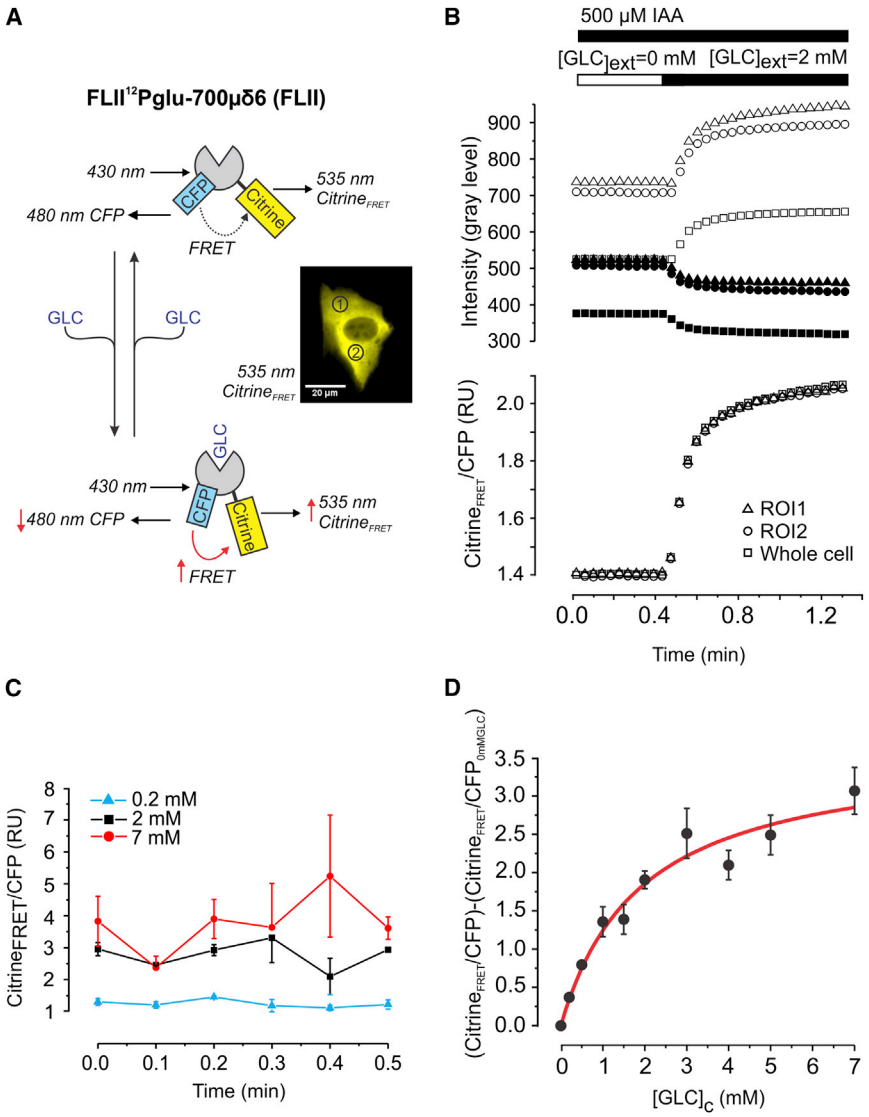

FIGURE 1 In situ calibration of the glucose sensor. (*A*) The glucose sensor FLII consists of a GLC binding domain that is sandwiched between CFP and Citrine. FRET increases and decreases upon GLC binding and unbinding to the sensor, respectively. The inset depicts a typical FLII-expressing C2C12 myoblast revealing the cytosolic localization of the sensor (Citrine image shown). ROIs used for temporal analysis of FLII fluorescence are marked by numerals. (*B*) Response of FLII to a stepwise increase in extracellular GLC ($[GLC]_{ext}$) in the presence of the GLC consumption inhibitor IAA. The top panel shows the individual CitrineFRET (*open symbols*) and CFP (*solid symbols*) average fluorescence intensity per pixel (*background corrected*) for the two ROIs indicated in (*A*). In addition, the average fluorescence intensity per pixel (*background corrected*) for the total cell was determined by creating a cellular mask (*binary image*) of the cell and superimposing this mask onto the background corrected image. Calculation of the FLII emission ratio ($Citrine_{FRET}$/CFP) revealed identical ratio-unit changes in all signals (*lower panel*). (*C*) Stability of the FLII ratio signal following 30 min incubation at various $[GLC]_{ext}$ in the presence of 500 μM IAA. FLII images of different cells were acquired. The mean Citrine-FRET/CFP signal ($\pm$SD) of all cells within individual images were plotted as a function of time for 0.2, 2, and 7 mM $[GLC]_{ext}$. For each concentration, no significant differences were detected between time points (one-way analysis of variance). (*D*) Average CitrineFRET/CFP signal ($\pm$SE) as a function of $[GLC]_{ext}$ (20 cells analyzed for each $[GLC]_{ext}$). Data were corrected by subtracting the FLII emission ratio obtained at $[GLC]_{ext} = 0$. A Michaelis-Menten equation was used to fit the calibration curve ($R^2 = 0.96$). To see this figure in color, go online.

(Fig. S1 in the Supporting Material). This suggests that V_1 is dominated by Glut1-mediated GLC entry in our C2C12 myoblasts. To dissect the contribution of V_1 and V_2 in determining $[GLC]_c$, we adapted a strategy previously described for cultured mouse astrocytes (35). Quantification of V_1 requires inhibition of GLC consumption, which was achieved using IAA (Fig. 2 *A*). Conversely, GLC entry was inhibited using cytochalasin B (CytoB) (Fig. 2 *A*), a noncompetitive and membrane-permeable inhibitor of Glut uniporters (17,33,35,38,39). CytoB inhibits GLC transport by binding close to the GLC efflux site on the cytoplasmic domain of Gluts (22,40). Control experiments demonstrated that CytoB indeed blocked Glut-mediated GLC influx in our cell system (Supporting Material B1 and Fig. S2 *A*). Removal of extracellular GLC induced a drop in $[GLC]_c$ to zero within 3 min (Fig. 2 *B*), suggesting that cytosolic GLC is actively consumed. When CytoB treatment was carried out on IAA-pretreated cells, the decrease in $[GLC]_c$ was blocked in a dose- and time-dependent manner. It was found that 15 min pretreatment with 500 μM IAA fully blocked GLC consumption (Fig. 2 *C*). The experimental strategy to measure V_1 in C2C12 myoblasts is schematically summarized in Fig. 2 *D* and allows analysis of GLC entry under zero-*trans* conditions (i.e., when $[GLC]_c$ is virtually zero before external GLC re-addition). It consists of cell seeding and transfection (Fig. 2, *Da* and *Db*), optional treatment with a mitochondrial inhibitor (Fig. 2 *Dc*; see below), removal of extracellular GLC (Fig. 2 *Dd*), IAA treatment (Fig. 2 *De*), and re-addition of external GLC (Fig. 2 *Dg*). In the absence of IAA, increasing $[GLC]_{ext}$ from 0 to 2 mM induced a biphasic increase in $[GLC]_c$ in GLC-depleted myoblasts (Fig. 2, *E* and *F*, *open symbols/bars*) consisting of a fast ($V_{1,No\text{-}IAA}$) and slow component ($V_{1slow,No\text{-}IAA}$). In myoblasts preincubated with IAA (500 μM, 15 min) the rate of fast $[GLC]_c$ increase ($V_{1,IAA}$) was significantly

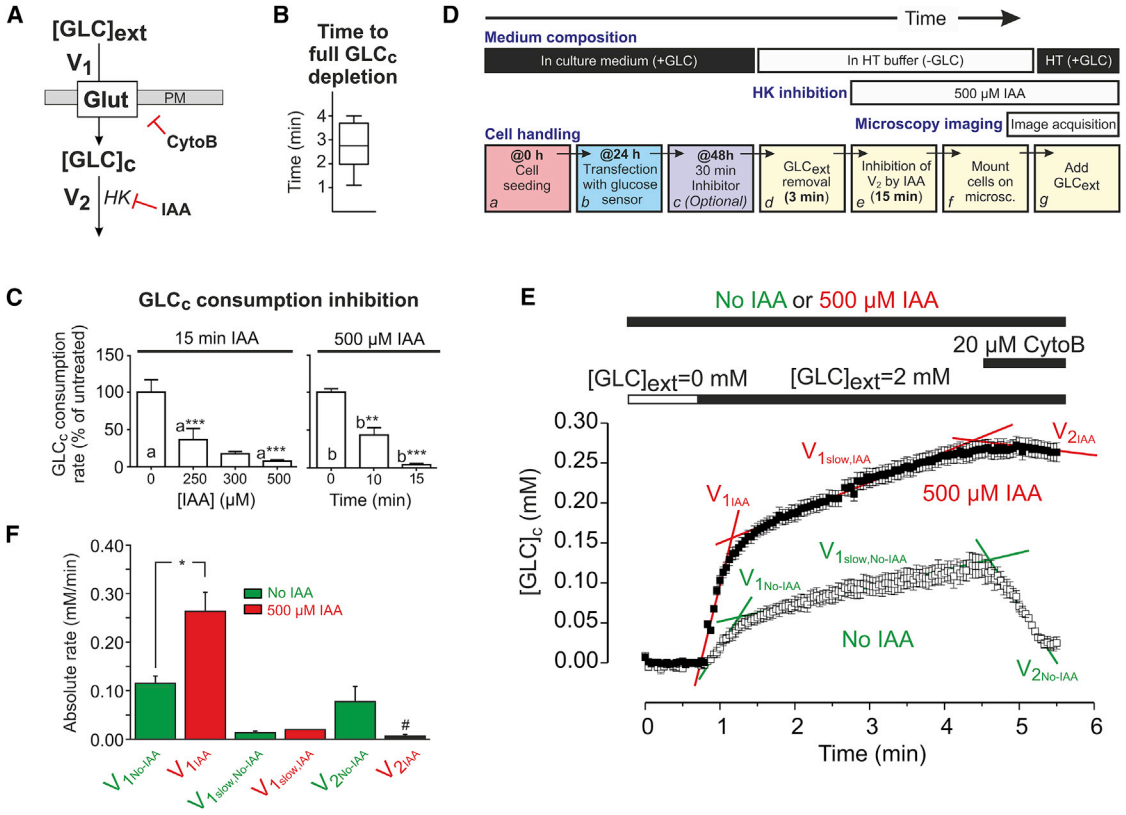

FIGURE 2 Experimental strategy for analysis of glucose uptake and consumption. (*A*) Principle of the approach. GLC enters from the extracellular space ($[GLC]_{ext}$) into the cytosol ($[GLC]_c$) via facilitative Glut across the PM and is subsequently consumed. GLC enters at a rate V_1 and is consumed at a rate V_2. CytoB and IAA (acting on HK) are used to inhibit V_1 and V_2, respectively. (*B*) Box plot of the average time required for lowering $[GLC]_c$ to zero upon removal of $[GLC]_{ext}$ ($n = 10$ cells; $N = 2$ independent experiments). (*C*) Analysis of the concentration and duration of IAA treatment required for full inhibition of GLC consumption. Graph presents the mean (±SE) of 15 cells per condition ($N = 3$ independent experiments). Statistical significance was determined using the Kruskal-Wallis test. (*D*) Flowchart of the experimental approach. After seeding and FLII transfection, cells are optionally treated with mitochondrial inhibitors for 30 min. Subsequently, ($[GLC]_{ext}$ is removed and V_2 is inhibited by IAA, followed by microscopy imaging. (*E*) Representative example of a GLC uptake experiment in the absence (*solid symbols*) and presence (*open symbols*) of IAA. After a 3 min incubation in the absence of extracellular GLC, $[GLC]_{ext}$ was increased to 2 mM followed by addition of CytoB. Both in the absence and presence of IAA, $[GLC]_c$ displayed a biphasic increase at rates $V_{1,No\text{-}IAA}$ and $V_{1,IAA}$ and $V_{1slow,No\text{-}IAA}$ and $V_{1slow,IAA}$ upon external GLC addition. The effect of CytoB was reflected by the rates $V_{2,No\text{-}IAA}$ and $V_{2,IAA}$. (*F*) Average values (±SD) for the various rates depicted in (*E*) (determined from linear regression analysis; $n = 12$ cells; $N = 3$ independent experiments). #Not significantly different from zero determined by a one-way Student's *t*-test. To see this figure in color, go online.

higher than $V_{1,No\text{-}IAA}$, whereas the rate of increase of the slow phase ($V_{1slow,IAA}$ vs. $V_{1slow,No\text{-}IAA}$) was not affected (Fig. 2, *E* and *F*). This shows that in the absence of IAA, V_1 is underestimated due to GLC consumption, primarily during the fast phase. In the absence of IAA, CytoB induced an acute drop in $[GLC]_c$ at a rate $V_{2,No\text{-}IAA}$ (Fig. 2, *E* and *F*). In contrast, no significant decrease in $[GLC_c]$ was observed (i.e., $V_{2,IAA}$ equaled zero) when CytoB was added to IAA-treated cells (Fig. 2, *E* and *F*). Supported by the results presented in Fig. 2 *C*, these findings show that GLC is not consumed in IAA-treated C2C12 cells. Applying Eq. 3 to the data presented in Fig. 2 *F* suggests that 1) in the presence of IAA: $V_2 \approx 0$ so $d[GLC]_c/dt = V_1 = V_{1,IAA} = 0.26 \pm 0.07(SD)$ mM/min, 2) in the absence of IAA, V_1 is underestimated by an amount of $V_{2,No\text{-}IAA}$, so $d[GLC]_c/dt = V_{1,No\text{-}IAA} + V_{2,No\text{-}IAA} = 0.12 \pm 0.03(SD) + 0.08 \pm 0.06(SD) = 0.20 \pm 0.07(SD)$ mM/min. The fact that $V_{1,IAA}$ is $\approx V_{1,No\text{-}IAA} + V_{2,No\text{-}IAA}$ strongly suggests that the effect of IAA on V_1 is due to inhibition of V_2 rather than an aspecific effect of this inhibitor on Glut1.

Effect of mitochondrial inhibition on cellular GLC uptake and consumption in C2C12 myoblasts

Using the strategy in Fig. 2 *D*, we next investigated the effect of short-term mitochondrial dysfunction on cellular GLC uptake and consumption. To this end, cells were incubated with mitochondrial inhibitors for 30 min before microscopy analysis. In these experiments PA was used to inhibit complex I (CI) of the OXPHOS system. In parallel experiments, cells were treated with AA to inhibit OXPHOS

CII. Respirometry analysis revealed that both inhibitors dose-dependently inhibited CI and CIII (Fig. S3). Full inhibition of mitochondrial O_2 consumption in intact C2C12 cells required a minimal concentration of 100 nM PA (IC_{50} = 8.4 ± 0.2 nM) and 20 nM AA (IC_{50} = 8.5 ± 0.2 nM). These concentrations were used during the remainder of the study. First, we quantified the effect of 30 min mitochondrial inhibition on the maximal rate of GLC entry for various $[GLC]_{ext}$ in IAA-treated cells (Fig. 3 *A*). This was performed by calculating the maximal linear rate of $[GLC]_c$ increase from single-cell recordings (Fig. 3 *B*), which increased as a function of $[GLC]_{ext}$ in vehicle-, PA-, and AA-treated cells (Fig. 3 *C*). Curve fitting using a Hill equation revealed that the V_1-associated K_m value (Fig. 3 *D*; Table 1, *A1*) and cooperativity factor n (Fig. 3 *E*) were not affected in PA- and AA-treated cells. In contrast, inhibitor-treated cells displayed a large increased in maximal value of V_1 ($V_{1,max}$) (Fig. 3 *F*; Table 1, *A1*).

We then analyzed the resting $[GLC]_c$ and the maximal linear rate of $[GLC]_c$ decrease upon acute CytoB treatment (Fig. 4, *A* and *B*). In the literature a K_m value of 60 μM was reported for HK (21,41). Because the steady-state value of $[GLC]_c$ was 7- to 10-fold higher than this value, we considered the maximal linear rate of $[GLC]_c$ decrease upon acute CytoB treatment to reflect the maximal value of V_2 ($V_{2,max}$). Inhibitor treatment did not significantly alter the resting $[GLC]_c$ at 2 mM $[GLC]_{ext}$ (Fig. 4 *C*; Table 1, *A3*), whereas $V_{2,max}$ was 1.8- and 2.5-fold higher in PA- and AA-treated cells, respectively (Fig. 4 *D*; Table 1, *A2*). Taken together, our results show that inhibition of CI and CIII increase the maximal rates of cellular GLC uptake ($V_{1,max}$) and consumption ($V_{2,max}$) within 30 min.

A minimal mathematical model for GLC uptake and consumption in C2C12 myoblasts

To gain insight into how V_1 and V_2 quantitatively contribute to the kinetics of the $[GLC]_c$ signal, we developed a mathematical model starting from Eq. 3. Because cellular volume changes were not observed (see above), cell volume in the model was assumed to be constant. Glut-mediated GLC influx (V_1) was modeled using an equation (41) that was

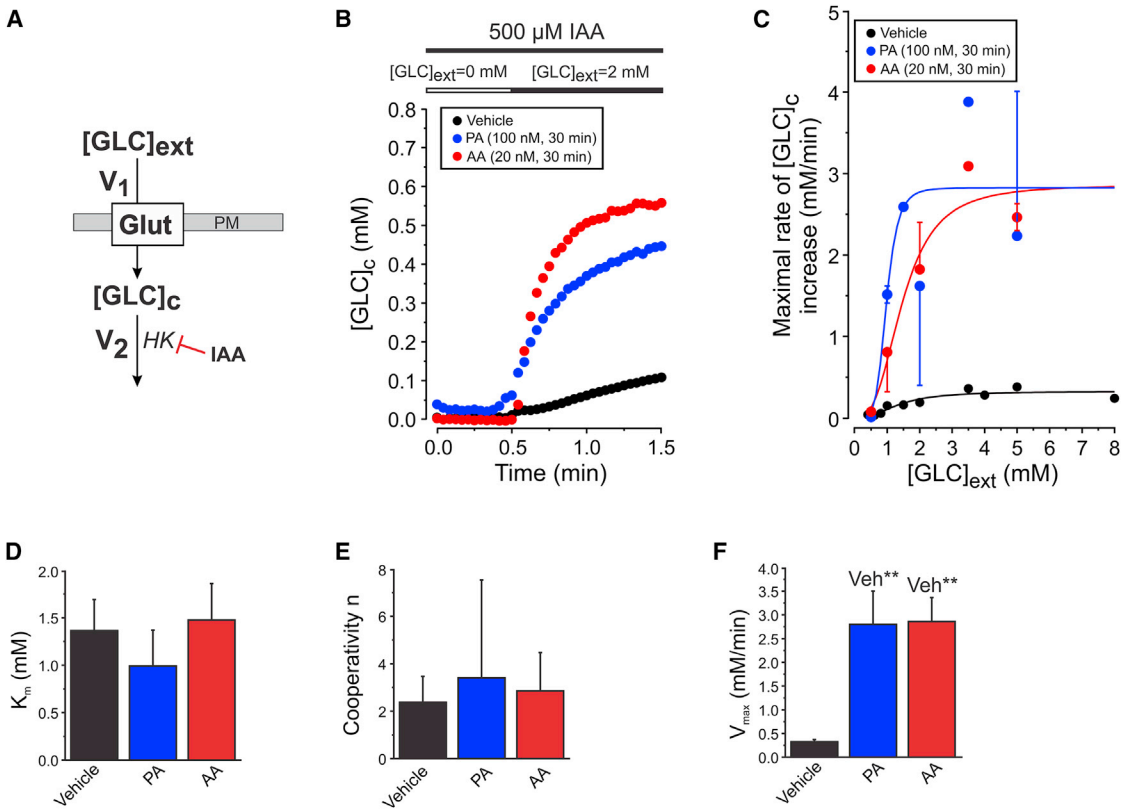

FIGURE 3 Effect of mitochondrial inhibition on cellular glucose uptake kinetics. (*A*) Inhibition of the GLC consumption flux (V_2) allows analysis of GLC uptake (V_1). (*B*) Typical GLC uptake in cells pretreated with vehicle, PA, or AA for 30 min. The maximal rate of linear increase of these curves was used as a measure of V_1. (*C*) Mean (±SE) of the maximal rate of $[GLC]_c$ increase as a function of $[GLC]_{ext}$ in vehicle-treated cells and cells treated with PA or AA ($n = 20$ cells per condition; $N = 4$ independent experiments). A Hill equation was used for curve fitting (Vehicle: $R^2 = 0.85$; PA: $R^2 = 0.68$; AA: $R^2 = 0.94$). (*D*) Average value (±SD) of K_m for vehicle-, PA-, or AA-treated cells. (*E*) Similar to (*D*), but now for the cooperativity parameter *n*. (*F*) Similar to (*D*), but now for V_{max}. To see this figure in color, go online.

TABLE 1 Experimental results, model parameters and model predictions

Parameter	Vehicle	PA	AA
A. Model Directly Based upon Experimental Parameters (Default Model)			
1) GLC uptake rate (V_1) parameters[a]			
Experimental $K_{m,V1}$ (mM)	1.4 ± 0.3	1.0 ± 0.4	1.5 ± 0.4
Experimental $V_{1,max}$ (mM/min)	0.32 ± 0.05	2.8 ± 0.7	2.9 ± 0.5
2) GLC consumption rate (V_2) parameters[b]			
Experimental $V_{2,max}$ (mM/min)	0.67 ± 0.07	1.23 ± 0.12	1.7 ± 0.3
$K_{m,V2}$ (mM)	0.06	0.06	0.06
3) $[GLC]_c$ at steady-state			
Experimental (mM)	0.49 ± 0.11	0.66 ± 0.09	0.51 ± 0.07
Predicted (mM)	0.02	0.40	0.20
B. Model with Adjusted $V_{1,max}$ (Optimal Model)			
1) GLC uptake rate (V_1) parameters			
Adjusted $V_{1,max}$ (mM/min)	1.86	4.20	4.80
2) $[GLC]_c$ at steady-state			
Predicted (mM)	0.49	0.66	0.51
3) GLC, PYR, LAC and ATP rates at steady-state[c]			
Predicted $V_1 = V_2 = V_{steady\text{-}state}$ (mM/min)	0.60	1.14	1.50
Predicted PYR production rate $V_3 = 2 \times V_{steady\text{-}state}$ (mM/min)	1.20	2.28	3.00
Predicted rate of LAC release $V_7 = V_4 = V_3$ (mM/min)[d]	1.20	2.28	3.00
Experimental rate of LAC release V_7 (mM/min/cell)	1.8 ± 0.6 (SD)	4.1 ± 1.1 (SD)	3.5 ± 1.6 (SD)
Predicted glycolytic ATP production rate $2 \times V_{steady\text{-}state}$ (mM/min)	1.20	2.28	3.00
Experimental ATP-linked O_2 consumption rate (mM/min)	0.43 ± 0.08 (SD)	0	0
Experimental P/O ratio	2.7 ± 0.4 (SD)	n.d.	n.d.
Predicted mitochondrial ATP production rate (mM/min)	1.2 ± 0.2 (SD)	0	0
Predicted total ATP production (mM/min)	2.39 (100%)	2.28 (95%)	3.00 (126%)
Experimental total ATP (pmol/cell)	30 ± 13 (SD)	19 ± 5 (SD)	30 ± 18 (SD)

All experiments and model predictions were performed at an extracellular free glucose concentration ($[GLC]_{ext}$) of 2 mM. Statistics: errors reflect SEM, unless stated otherwise. the number of cells analyzed and experiments performed is provided in the figure legends. Abbreviations: AA, antimycin A; GLC, glucose; $K_{m,V1}$, affinity (K_m) of GLC uptake; $K_{m,V2}$, affinity (K_m) of GLC consumption; LAC, lactate; PA, piericidin A; SD, standard deviation; $V_{1,max}$, maximal rate (V_{max}) of GLC uptake; $V_{2,max}$, maximal rate (V_{max}) of GLC consumption.

LAC production was measured during 60–90 min in three independent experiments. Routine O_2 consumption and P/O ratio were determined in four independent experiments. Total ATP after 24 h incubation with vehicle, PA, or AA was measured in three independent experiments, performed in duplo.

[a]Measured under conditions of IAA-blocked GLC consumption.

[b]Measured under conditions of CytoB-blocked GLC uptake.

[c]Average C2C12 cell volume equaled $2.1 \times 10^{-12} \pm 0.4 \times 10^{-12}$ (SD) L ($n = 14$ cells).

[d]Assuming a negligible magnitude for V_5.

previously used for quantitative prediction of Glut1-mediated GLC influx in HepG2 cells (22):

$$V_1 = Flux_{out \rightarrow in} = \frac{V_{1,max} \times \left([GLC]_{ext} - [GLC]_c\right) \times K_{m,V1}}{\left(K_{m,V1} + [GLC]_{ext}\right) \times \left(K_{m,V1} + [GLC]_c\right)}, \quad (4)$$

with $V_{1,max}$ being the measured maximal value of V_1 (Table 1, *A1*; in mM/min), $K_{m,V1}$ the measured affinity (Table 1, *A1*; in mM), $[GLC]_{ext}$ the extracellular free GLC concentration (in mM) and $[GLC]_c$ the cytosolic free GLC concentration (in mM). We modeled cytosolic GLC consumption (V_2) using a Michaelis-Menten equation (42) that quantitatively predicted HK-mediated GLC consumption in HepG2 cells (33):

$$V_2 = \frac{V_{2,max} \times [GLC]_c}{K_{m,V2} + [GLC]_c}, \quad (5)$$

with $V_{2,max}$ being the measured maximal value of V_2 (Table 1, *A2*; in mM/min), $K_{m,V2}$ the affinity (in mM), and $[GLC]_c$ the cytosolic free GLC concentration (in mM). Under conditions that GLC influx is blocked, the rate at which $[GLC]_c$ drops will reflect maximal HK action (see above) so we used a $K_{m,V2}$ value of 60 μM (Table 1, *A2*) as described in the literature (21,43).

Parameter optimization and validation of the mathematical model

Using the experimental parameter values for V_1 and V_2 (Table 1) we performed a set of explorative simulations for the vehicle condition at 2 mM $[GLC]_{ext}$. This default model quantitatively matched (not shown) the experimental data obtained in vehicle-, PA-, and AA-treated cells, with respect to maximal rate of $[GLC]_c$ decrease. This suggests that the kinetic parameters measured for V_2 were correct for all three conditions. However, the default model

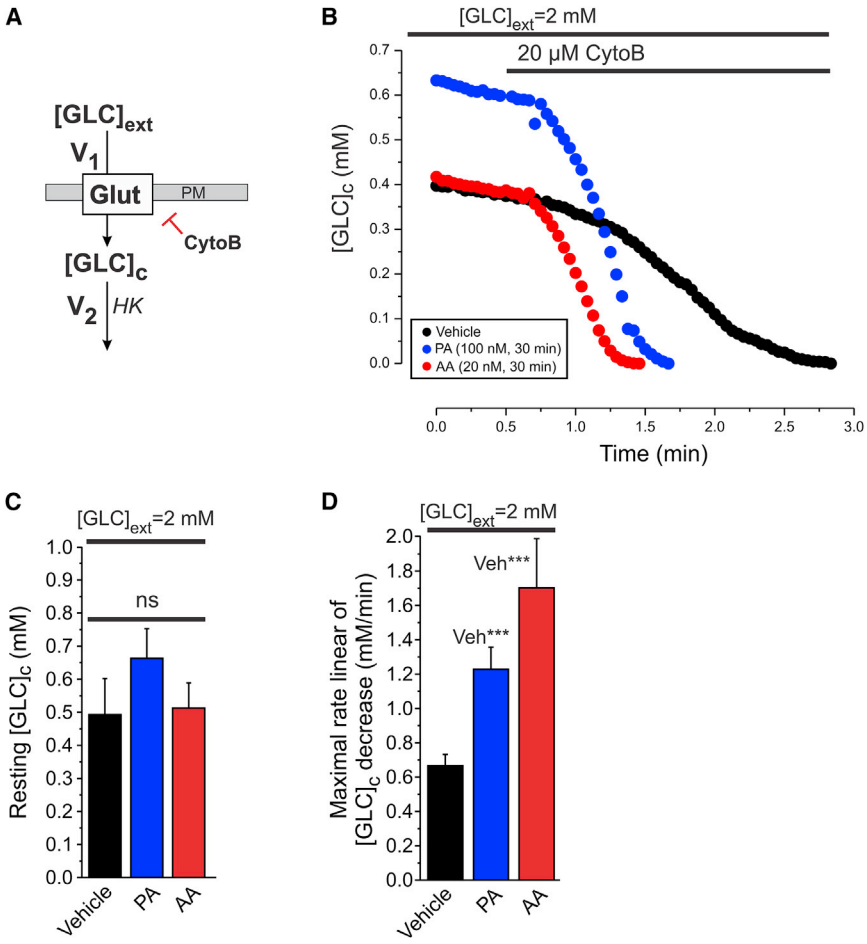

FIGURE 4 Effect of mitochondrial inhibition on cellular glucose consumption kinetics. (*A*) Inhibition of the GLC uptake flux (V_1) allows analysis of GLC consumption (V_2). (*B*) Typical glucose consumption experiment in cells treated with vehicle, PA, or AA for 30 min. (*C*) Average value (±SD) of resting $[GLC]_c$ for 2 mM $[GLC]_{ext}$ in the absence of CytoB for vehicle-, PA-, or AA-treated cells (*D*) The average value (±SD) of the maximal rate of linear decrease upon cytoB addition in (*B*). V_2 ($n = 20$ cells; $N = 4$ independent experiments). N.s. not significant. To see this figure in color, go online.

predicted a much lower steady-state $[GLC]_c$ (i.e., 0.02 mM) than the experimental value (0.49 mM) (Table 1, *A3*). To gain insight into why the predicted steady-state $[GLC]_c$ was much lower, the V_1 parameters (i.e., $K_{m,V1}$, $K_{m,V2}$ $V_{1,max}$, $V_{2,max}$) were manually varied in the default model to fit the experimental steady-state $[GLC]_c$. This revealed that only when $V_{1,max}$ was increased (i.e., from 0.32 to 1.86 mM/min), the predicted steady-state $[GLC]_c$ matched its experimental value. Also, for the PA- and AA-treated condition, the steady-state $[GLC]_c$ predicted by the default model was too low (Table 1, *A3*). This discrepancy disappeared when $V_{1,max}$ was increased from 2.8 to 4.2 mM/min (PA-treated cells) and from 2.9 to 4.8 mM/min (AA-treated cells). In this way, optimal models were obtained (Table 1, *B*). Upon simulating the FLII calibration procedure, the optimal model correctly predicted the experimental calibration curve (Supporting Material B2 and Fig. S5, *A* and *B*). The too low $V_{1,max}$ values reported in our experiments might be because the rate of GLC uptake was determined under conditions of virtually zero $[GLC]_c$ (zero-trans condition; (44)). This would lead to an underestimation of $V_{1,max}$ because $[GLC]_c$ stimulates Glut-mediated GLC influx by a mechanism called *trans*-acceleration (45,46). Indeed (Fig. S4, *A* and *B*), the maximal rate of $[GLC]_c$ increase was much higher when [GLC]c equaled 0.4 mM (i.e., when GLC uptake was *trans*-accelerated) than when $[GLC]_c$ was virtually zero (zero-*trans* condition). In this sense, the model-predicted underestimation of $V_{1,max}$ in our experiments is very likely due to the use of zero-*trans* conditions.

Model prediction of steady-state GLC uptake and consumption

In a first set of simulations we used the optimal model to simulate the experiment in Fig. 4 *B*. Model predictions (Fig. 5 *A*) quantitatively matched the experimental data obtained in vehicle-, PA-, and AA-treated cells, with respect to resting $[GLC]_c$ (Fig. 4 *C*) and maximal rate of $[GLC]_c$ decrease (Fig. 4 *D*). We then simulated the experiment in Fig. 2 *E*, to predict the steady-state values of V_1 and V_2 (Fig. 5 *B*). In the presence of 2 mM $[GLC]_{ext}$, V_1 and V_2 steady-state values (i.e., when $V_1 = V_2 = V_{steady\text{-}state}$) increased from 0.60 mM/min (vehicle) to 1.14 mM/min (PA) to 1.50 mM/min (AA), without significantly affecting steady-state $[GLC]_c$ (Fig. 4 *C*). To quantify the effect of V_1 and V_2 upon the overall steady-state GLC flux we

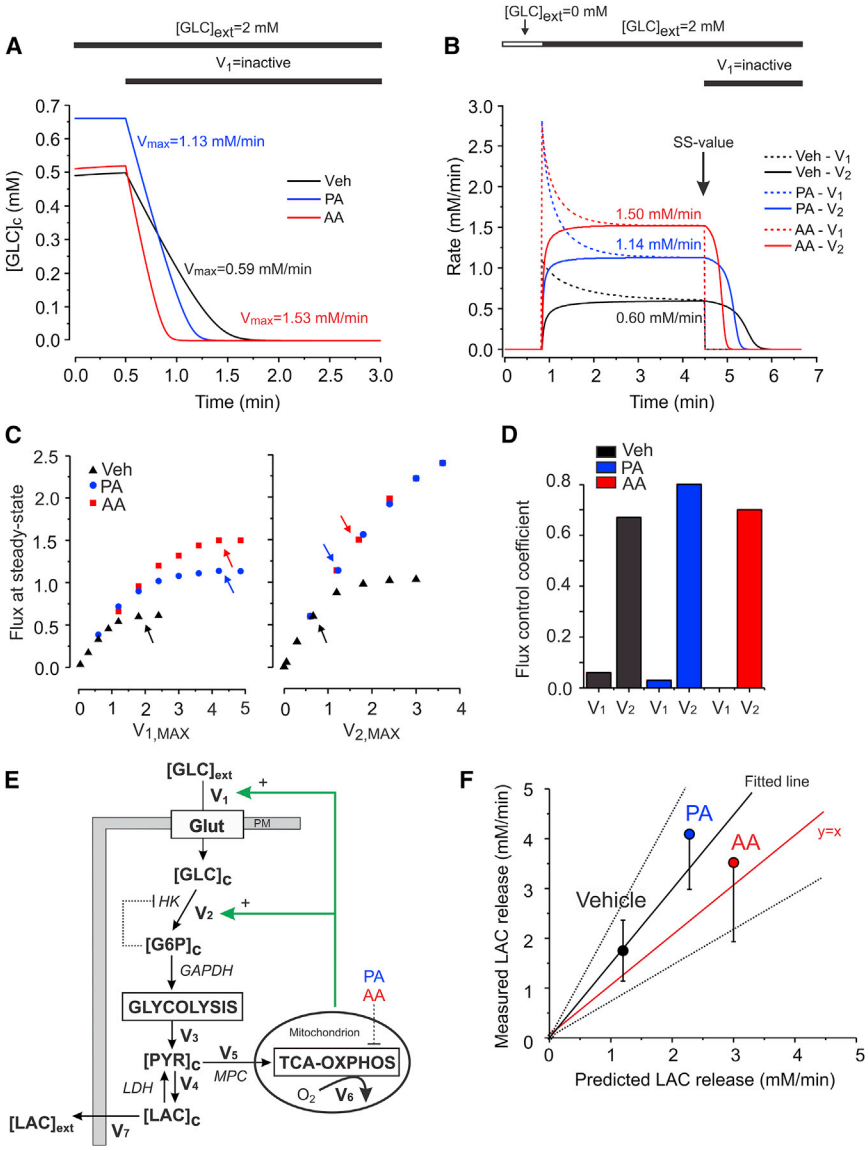

FIGURE 5 A minimal model of glucose uptake and consumption in C2C12 myoblasts. (*A*) $[GLC]_c$ dynamics predicted by the optimal models mimicking the experiments in Fig. 4 *B* for vehicle-, PA-, and AA-treated cells. Glucose influx (V_1) was set to zero to simulate Glut inhibition by CytoB. Both resting $[GLC]_c$ (*y* axis) and maximal linear rate of $[GLC]_c$ decrease (*numerals*) were predicted correctly. (*B*) Simulated experiment of Fig. 2 *E* to predict the steady-state values (*numerals*) of GLC influx (V_1; *dotted lines*) and consumption (V_2; *continuous lines*) in vehicle-, PA-, and AA-treated cells. Glucose influx (V_1) was set to zero to simulate Glut inhibition by CytoB. SS indicates the steady-state situation. (*C*) Flux variation as a function of $V_{1,max}$ and $V_{2,max}$. The steady-state flux at 2 mM GLC_{ext} was predicted for different values of $V_{1,max}$ (*left panel*) and $V_{2,max}$ (*right panel*). Arrows mark the V_{max} value in the respective models. (*D*) Flux control coefficients for V_1 and V_2 in (*C*) (see Results for details). (*E*) Schematic representation of the various fluxes (V_1, V_2, V_3, V_4, V_5, V_6, V_7; see Results and Discussion for details). (*F*) Comparison between the predicted single-cell LAC production flux (*x* axis) and measured average (±SD) of LAC production flux (*y* axis) in cells treated with vehicle, PA, or AA in HT buffer containing 2 mM GLC ($N = 3$ independent experiments). A linear equation was used for fitting ($R^2 = 0.90$; slope = 1.49 ± 0.29; dotted lines indicate 95% confidence limits). To see this figure in color, go online.

calculated flux control coefficients in the vehicle-, PA- and AA- model (Fig. 5, *C* and *D*). This was performed by determining the steady-state GLC flux values at various magnitudes of $V_{1,max}$ or $V_{2,max}$ (27,47). The arrows in Fig. 5 *C* indicate the values of $V_{1,max}$ (*left panel*) and $V_{2,max}$ (*right panel*) in the three optimal models. At each arrow we calculated the derivative to obtain the flux control coefficient (i.e., $d\ln(Flux/dV_{max}) = [dFlux/dV_{max}] \times [V_{max}/Flux]$). For all three steady-state conditions, the flux control coefficient was much larger for V_2 than for V_1 (Fig. 5 *D*), showing that the steady-state GLC flux is primarily determined by the steady-state value of V_2.

Model prediction of steady-state LAC production

Mitochondrial O_2 consumption was fully blocked in inhibitor-treated cells (Fig. S3). This suggests (Fig. 5 *E*) that the rate of mitochondrial PYR entry (V_5) is close to zero and that PYR (generated by glycolysis at a rate V_3) is converted into LAC at a rate V_4 and subsequently released by the cells at a rate V_7. Although IAA did not alter cytosolic pH, PA-, and AA-treatment acidified the cytosol to a similar extent (Fig. S2 *C*). Of importance, this acidification did not affect the FLII fluorescence signal (Supporting Material B1 and Fig S2, *B–D*). Assuming that all consumed GLC is converted into LAC that is transported out of the cell, we used the predicted $V_{steady\text{-}state}$ to calculate V_7. At 2 mM $[GLC]_{ext}$ the optimal model predicts (Table 1, *B3*) that $V_{steady\text{-}state}$ equals 1.14 mM/min (PA) and 1.50 mM/min (AA). Because glycolytic conversion yields two PYR molecules for each GLC molecule that is consumed, the predicted rates of PYR generation (V_3) and LAC release (V_7) equal $V_3 = V_7 = 2 \cdot V_{steady\text{-}state}$, yielding 2.3 mM/min (PA) and 3.0 mM/min (AA). Experimental analysis (using the

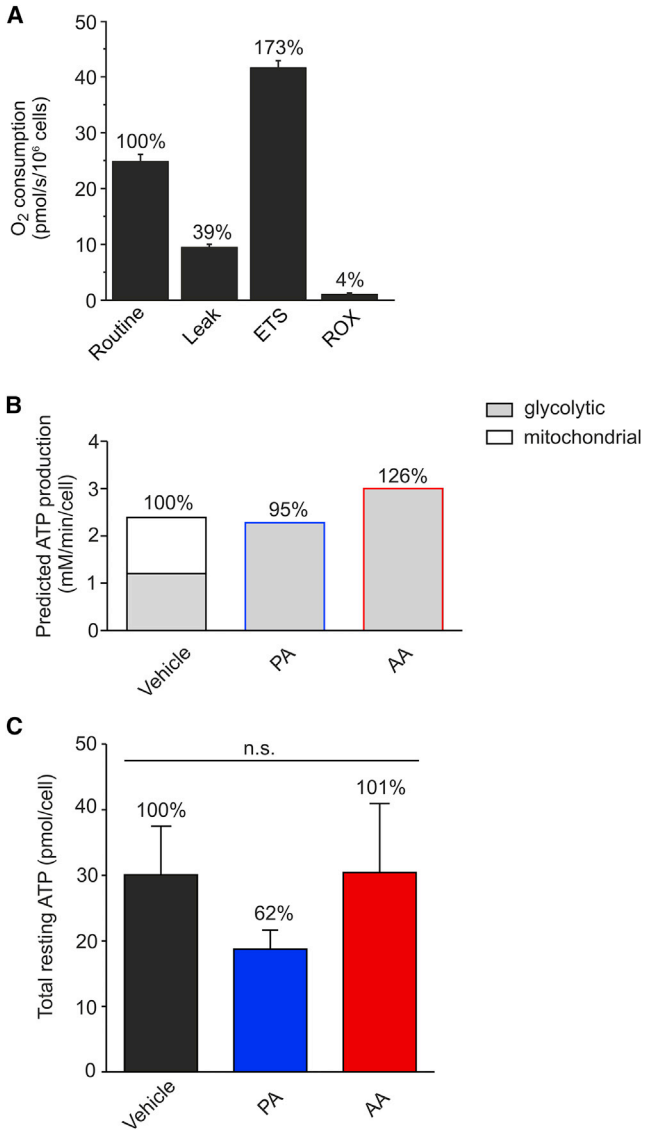

FIGURE 6 Analysis of O_2 consumption and total cellular ATP levels in C2C12 myoblasts. (*A*) Average values (±SE) for routine, leak, maximal (ETS) and residual respiration (ROX) in C2C12 cells ($N = 6$ independent experiments). (*B*) Predicted balance between glycolytic and mitochondrial ATP production in vehicle- and inhibitor-treated cells. See Results for details. (*C*) Average values (±SE) of total ATP levels in cells treated for 24 h with vehicle, PA, or AA ($N = 3$ independent experiments). Statistical significance was assessed using the Kruskal-Wallis test. To see this figure in color, go online.

same medium used for FLII imaging) yielded LAC fluxes of 3.7 ± 1.1 (SD) fmol/min/cell (vehicle), 8.7 ± 1.5 (SD) fmol/min/cell (PA), and 7.5 ± 3.0 (SD) fmol/min/cell (AA). To compare these experimental values with the predictions of the mathematical model (which simulates a single cell) information about C2C12 myoblast volume is required. To this end, we first determined the area of FLII-expressing cells (using the $Citrine_{FRET}$ image), yielding an average value of $1.2 \times 10^3 \pm 0.4 \times 10^3$ (SD) μm^2 ($n = 14$ cells). Using data from the literature (48) it was found that C2C12 area and volume display a highly linear correlation (Fig. S6). From this correlation we estimated that the average C2C12 volume in our experiments equaled $2.1 \times 10^{-12} \pm 0.4 \times 10^{-12}$ (SD) L, compatible with a previous estimate obtained by three-dimensional microscopy analysis (49). In case of PA-treated cells the measured value of V_7 equaled (8.7 ± 1.5 fmol/min/cell)/($2.1 \times 10^{-12} \pm 0.4 \times 10^{-12}$ L) = 4.1 ± 1.1 mM/min/cell. A similar calculation yields 1.8 ± 0.6 mM/min/cell and 3.5 ± 1.6 mM/min/cell for vehicle- and AA-treated cells, respectively. Quantitative comparison of these measured LAC fluxes with model predictions revealed a linear correlation (Fig. 5 *F*). The fitted line did not significantly differ from $y = x$ (i.e., the latter fell within the 95% confidence limits of the fitted line), suggesting that the model correctly predicted LAC fluxes (V_7) for vehicle- and inhibitor-treated cells.

Model predictions of steady-state ATP production

Finally, we integrated model predictions and experimental results to analyze the balance between glycolytic and mitochondrial ATP production in C2C12 cells. For vehicle-treated cells the amount of ATP derived from glycolysis equaled $2 \cdot V_{steady\text{-}state}$ (i.e., 1.20 mM/min). To compare this flux with mitochondrial ATP production, we measured routine O_2 consumption (Fig. 6 *A*). Following correction for leak respiration, the ATP-linked O_2 consumption rate equaled 15.4 ± 2.7 pmol/s/10^6 cells. Considering C2C12 cell volume, this yields an ATP-linked O_2 flux of 0.43 ± 0.08 (SD) mM/min (Table 1, *B3*). The ATP production rate was then calculated from this O_2 flux using the phosphorus/oxygen ratio (P/O ratio). The latter was determined by measuring the amount of O_2 required to convert 220 nmol ADP to ATP in permeabilized cells supplemented with PYR and malate (50). This strategy revealed a P/O ratio of 2.7 ± 0.4 (SD) (Table 1, *B3*; Fig. S7), meaning that ATP is produced by mitochondria at a rate of (2.7 ± 0.4) × (0.43 ± 0.08 mM/min) = 1.2 ± 0.2 (SD) mM/min. Therefore, vehicle-treated C2C12 cells derive 50% of their cellular ATP from glycolysis and 50% from OXPHOS (Fig. 6 *B*; Table 1, *B3*). For inhibitor-treated cells we assumed that ATP is exclusively generated by glycolysis, yielding fluxes of 2.28 mM/min (PA) and 3.00 mM/min (AA). Therefore, the total steady-state ATP production flux is virtually identical for vehicle- and inhibitor-treated cells (Fig. 6 *B*): 2.39 mM/min (vehicle, set at 100%), 2.28 mM/min (PA; 95%), and 3.00 mM/min (AA; 126%). In line with these predictions, 24 h treatment with vehicle-, PA and AA did not significantly affect the total cellular ATP level (Fig. 6 *C*; Table 1, *B3*) or the total number of cells (data not shown). This suggests that increased steady-state GLC uptake and consumption fully compensates for the loss of mitochondrial ATP production in PA- and AA-treated cells.

DISCUSSION

This study focuses on gaining a quantitative understanding of the balance between steady-state GLC uptake/consumption, glycolytic, and mitochondrial ATP production, and the effect of mitoenergetic dysfunction on this system. We provide integrated experimental and in silico evidence that the glycolytic pathway and mitochondria equally contribute to total ATP production in C2C12 myoblasts. Acute (30 min) OXPHOS inhibition induced a twofold increase in steady-state GLC uptake and consumption, which fully compensated for the drop in mitochondrial ATP production. Our results suggest a mechanism in which mitoenergetic dysfunction triggers compensatory activation of the glycolysis pathway, allowing metabolic flexibility.

In situ calibration and validation of the FLII GLC sensor

Predictive mathematical modeling requires a quantitative measure of $[GLC]_c$. Therefore, we calibrated the emission ratio of the FLII sensor by incubating the cells with different $[GLC]_{ext}$ concentrations in the presence of the V_2 inhibitor IAA. The in situ FLII calibration curve displayed Michaelis-Menten kinetics and a K_m of 1.9 mM, which was 2.7-fold higher than its in vitro K_m value (51). This illustrates the importance of in situ calibration (52) and demonstrates that FLII most sensitively reports $[GLC]_c$ when $[GLC]_c$ is near 1.9 mM. Of note, discrepancies between in situ and in vitro K_m values are not uncommon, as illustrated by the eightfold increase in K_m for the proteinaceous Ca^{2+} sensor PericamR when expressed in the mitochondrial matrix (53). We demonstrated that the FLII ratio is not affected by cytosolic acidification in our experiments, compatible with previous findings in yeast cultures (51). Taken together, we provided evidence that the employed calibration procedure and experimental conditions are suited for quantitative measurement of $[GLC]_c(t)$ using the FLII sensor.

Quantification of cellular GLC uptake and consumption

In previous studies cellular GLC uptake (V_1) was measured using a radio-labeled variant of GLC (i.e., 2-deoxy-D-glucose or 2DG), which inhibits HK and is phosphorylated by this enzyme (54,55). However, this approach cannot be used to study the relatively rapid temporal GLC dynamics at the (sub)cellular level. In addition, fluorescently labeled GLC analogs such as 2-(*N*-(7-nitrobenz-2-oxa-1,3-diazol-4-yl)amino)-2-deoxyglucose (2-NBDG) and 6-(*N*-(7-nitrobenz-2-oxa-1,3-diazol-4-yl)amino)-6-deoxyglucose (6-NBDG) have been used to quantify V_1 (56,57). However, these GLC analogs display a different affinity for Glut transporters than GLC (58). Here, we experimentally dissected the contribution of V_1 to $[GLC]_c$ dynamics, by removing $[GLC]_{ext}$ and preventing cytosolic GLC consumption (V_2) using IAA. Measurements of zero-*trans* GLC uptake were performed by extracellular addition of GLC to cells with zero GLC on the *trans* (i.e., intracellular) site. Upon GLC addition, the rate of change in $[GLC]_c$ (i.e., $d[GLC]_c/dt$) was determined by quantifying the maximal slope of the calibrated FLII signal. This slope was then used as a measure of the initial rate of GLC uptake. Because the sum of V_1 and V_2 in the absence of IAA is similar to the experimental value of V_1 in the presence of IAA, it appears that IAA does not affect GLC uptake. Q-PCR analysis revealed that Glut1 is expressed, whereas Glut2, Glut3, and Glut4 transcripts were not detected. This suggests that V_1 primarily reflects Glut1-mediated GLC uptake. In vehicle-treated cells the maximal rate of V_1 ($V_{1,max}$) was 0.32 $\pm$ 0.05 mM/min and its K_m value ($K_{m,V1}$) equaled 1.4 $\pm$ 0.3 mM. Similar $K_{m,V1}$ values (i.e., 0.38–2.00 mM) were reported in previous studies (22,28,44,59), suggesting that our experimental strategy to determine $K_{m,V1}$ is valid. The maximal value of V_2 ($V_{2,max}$) was determined in the presence of the V_1-blocker CytoB (35). Because HK displays a GLC-affinity of ~60 μM (7,43) it operates (near) it's V_{max} at the measured $[GLC]_c$ concentrations.

OXPHOS inhibition stimulates cellular GLC uptake

30 min treatment with PA or AA did not significantly affect the affinity of GLC uptake ($K_{m,V1}$) but induced an eightfold increase in $V_{1,max}$, compatible with previous results in OXPHOS-inhibited cells (9,23,40,60,61). Similar to another study (62), Q-PCR analysis revealed that inhibitor treatment did not alter Glut mRNA levels (data not shown). Although PA and AA are chemically dissimilar and target different OXPHOS complexes, they equipotentially stimulated GLC uptake. This suggests that the latter is due to OXPHOS inhibition rather than off-target effects of PA and AA, supporting a mechanism in which acute mitochondrial dysfunction stimulates Glut1-mediated GLC uptake in C2C12 myoblasts. A similar phenomenon was induced by extracellular alkalinization, possibly by modification of Glut cysteine residues (63). However, here we measured that OXPHOS inhibition lowered cytosolic pH and increased extracellular LAC levels, which argues against involvement of alkalinization-induced Glut1 activation. Alternatively, OXPHOS inhibition might induce a drop in ATP level leading to reduced ATP-induced inhibition of Glut1 activity (64,65). Our results argue against such a mechanism because 1) they suggest that the drop in OXPHOS-mediated ATP production is fully compensated for by increased glycolytic activity, and 2) they demonstrate that total cellular ATP amount is not significantly reduced in cells treated with OXPHOS inhibitors for 24 h. Glut1 activity might also be increased by a mechanism involving AMP-activated protein kinase, activation (phosphorylation) of which was linked to stimulation of

GLC transport during OXPHOS inhibition (9,67). Alternatively, Glut1 redox modification and oligomerization were demonstrated to regulate Glut1 activity (68–71) and the amount of active Glut1 at the PM might be increased by stimulation of Glut1 translocation from internal storage vesicles to the PM or by activation of PM-localized Glut1 by OXPHOS inhibition (9–11,13).

OXPHOS inhibition stimulates cellular GLC consumption

OXPHOS inhibition induced a two-fold increase in the maximal rate of GLC consumption ($V_{1,max}$). Genomic expression profiling (http://www.ncbi.nlm.nih.gov/geo/; GEO accession: GDS2420) suggests that C2C12 myoblasts express HK isoforms I and II. HK-mediated phosphorylation of GLC leads to formation of G6P, which allosterically inhibits HKI and HKII. In case of HKI this inhibition is antagonized by P_i, whereas the latter activates HKII (72). This suggests that increased GLC consumption might be explained by P_i-induced activation of HKII during OXPHOS inhibition. However, as discussed previously, our results argue against such a mechanism because glycolytic activity fully compensated for the loss in OXPHOS-mediated ATP production in PA- or AA-treated cells and total cellular ATP was not affected after 24 h inhibitor treatment. GLC consumption might also be increased in OXPHOS-inhibited cells by activation of glucokinase, a low-affinity (K_m = 8 mM) HK isozyme (73). However: 1) the above expression profiling suggests that glucokinase is not expressed in C2C12 myoblasts (confirmed in (74)), and 2) the steady-state resting $[GLC]_c$ was 10-fold lower than the K_m of glucokinase in vehicle-treated and OXPHOS-inhibited cells. In addition to HK activation, increased GLC consumption likely involves stimulation of other (glycolytic) enzymes including phosphofructokinase (PFK) and pyruvate kinase. A more detailed analysis of the mechanism linking OXPHOS inhibition to activation of GLC uptake and consumption is currently carried out in our laboratory.

A minimal model of cytosolic GLC dynamics

To predict steady-state GLC uptake and consumption fluxes, we constructed a minimal mathematical model that consisted of two equations: 1) a reversible Michaelis-Menten equation for GLC uptake (V_1) and 2) an irreversible Michaelis-Menten equation for GLC consumption (V_2). The GLC uptake equation does not account for asymmetry (i.e., different kinetic parameters for GLC influx and efflux) or *trans*-accelerated transport. The kinetic parameters for V_1 ($K_{m,V1}$ and $V_{1,max}$) and V_2 ($V_{2,max}$) were experimentally determined and included in the model. In the case of V_2, we used a GLC-affinity ($K_{m,V2}$) of 60 μM compatible with values previously reported for HK and HK-mediated GLC consumption in C2C12 cells (22,35,43). Initially, the model predicted a too low steady-state $[GLC]_c$ in vehicle- and inhibitor-treated cells (default model). Manual parameter optimization revealed that our experimental strategy systematically underestimated $V_{1,max}$, which had to be increased from 0.32 to 1.86 mM/min (vehicle), from 2.8 to 4.20 mM/min (PA), and from 2.9 to 4.80 mM/min (AA) to generate quantitatively correct predictions (optimal model). Triggered by these model predictions, we provided experimental evidence suggesting that our experimental method underestimates the rate of GLC uptake due to a lower $[GLC]_c$. Of importance, the adjusted $V_{1,max}$ values in the optimal model fell within a similar range as those reported for Glut1-mediated GLC entry in HepG2 cells (i.e., 7.2 mM/min; (22)).

Predicting the glycolytic flux at steady-state

Model predictions yielded a steady-state value of $V_1 = V_2 = V_{steady\text{-}state}$ of 0.60 mM/min in vehicle-treated cells. $V_{steady\text{-}state}$ was twofold higher in PA- and AA-treated cells. Under all three conditions V_2 displayed the largest flux control coefficient (i.e., 0.6–0.8), indicating that the GLC flux was primarily determined by the steady-state value of V_2. The flux control coefficient of V_1 was below 0.1 for all three conditions. In comparison, the flux control coefficient of GLC uptake upon oxygen consumption ranged between 0.3 and 0.5 and increased upon lowering GLC_{ext} in *Trypanosoma brucei* (75). In PA- and AA-treated cells mitochondrial O_2 consumption was fully blocked, meaning that mitochondrial PYR entry (V_5) is negligible. Under these conditions, we assumed that all the GLC (consumed at rate $V_{steady\text{-}state}$) is converted into LAC and released from the cell at a predicted rate V_7. The latter prediction agreed with LAC release measurements, supporting the validity of our minimal model and suggesting that the contribution of alternative pathways branching off or feeding into to the glycolytic pathway is relatively low. Interestingly, also in the absence of inhibitors (i.e., when V_5 was not zero) the predicted V_7 was close to the measured LAC release. This strongly suggests that the magnitude of steady-state mitochondrial PYR uptake (V_5) is much smaller than the rate of PYR-to-LAC conversion (V_4) and subsequent LAC release (V_7) in vehicle-treated cells. Because the LAC release predicted using $V_{steady\text{-}state}$ matched with the experimental LAC release rate it appears that $V_{steady\text{-}state}$ is a good measure of GLC flux. The fact that the measured LAC release was higher than the predicted LAC release for all three conditions might be due to hydrolysis of glycogen to G6P, thereby increasing V_3 and V_7. In addition, we cannot exclude that glucogenic amino acids contribute to PYR and LAC production in our experiments. For analysis of the glycolytic flux, our strategy provides an alternative to measurement of the extracellular acidification rate, which

might not always provide a reliable estimate of glycolytic flux (76).

Balancing glycolytic and mitochondrial ATP production

Analysis of ATP-linked mitochondrial O_2 consumption and P/O ratio in vehicle-treated cells suggested that ATP was generated by the OXPHOS system at a rate of 1.20 mM/min. Because $V_{steady\text{-}state}$ also equaled 1.20 mM/min, this means that under vehicle conditions 50% of the total ATP is generated by glycolysis and 50% by OXPHOS. As a consequence, a twofold increase in $V_{steady\text{-}state}$ under conditions of OXPHOS inhibition fully compensates for the loss in OXPHOS-mediated ATP production. Indeed, model predictions suggested that the total cellular ATP production rate under steady-state conditions equaled 100% (vehicle), 95% (PA), and 126% (AA). Following 24 h treatment, total cellular ATP content and total cell number were similar for vehicle- and inhibitor-treated cells. This is compatible with a mechanism in which glycolytic ATP production fully compensates for the loss in mitochondrial ATP production. A similar lack of effect on total ATP content was demonstrated in MEFs from *NDUFS4*$^{-/-}$ mice with isolated CI deficiency (4) and in fully glycolytic skin fibroblasts treated for 72 h with the CI inhibitor rotenone (77). C2C12 myoblasts displayed a relatively high glycolytic and low mitochondrial PYR influx. This allowed a twofold increase in glycolytic flux to fully compensate for the lack of mitochondrial ATP production in PA- and AA-treated cells. In this context, cells displaying a more oxidative metabolism would likely require a larger increase in glycolytic flux to meet their overall ATP demand.

CONCLUSIONS

By combining experiments and mathematical modeling we demonstrate here that mitoenergetic dysfunction triggers a rapid compensatory increase in steady-state GLC uptake and consumption in C2C12 myoblasts. This mechanism maintains the balance between cellular ATP supply and demand, thereby preventing energy crisis in cells in which mitochondrial ATP generation is compromised.

SUPPORTING MATERIAL

Supporting Materials and Methods, Supporting Results, and seven figures are available at http://www.biophysj.org/biophysj/supplemental/S0006-3495(15)00784-5.

AUTHOR CONTRIBUTIONS

D.C.L.A. and W.J.H.K. designed the experiments. D.C.L. and T.J.J.S. performed the experiments. D.C.L.A., F.G.M.R., P.H.G.M.W., and W.J.H.K. wrote the article. W.J.H.K. supervised the research.

ACKNOWLEDGMENTS

We thank Dr. Lionel Blanchet (Department of Biochemistry 286) for assistance with data analysis and Jan Verhagen (Department of Clinical Chemistry, Radboud University Medical Center) for performing lactate measurements.

This work was supported by equipment grants of ZonMW (Netherlands Organization for Health Research and Development, No. 903-46-176), NWO (Netherlands Organization for Scientific Research, No. 911-02-008), and by the CSBR (Centres for Systems Biology Research) initiative from ZonMW (grant No. CSBR09/013V).

REFERENCES

1. Mitchell, P. 1961. Coupling of phosphorylation to electron and hydrogen transfer by a chemi-osmotic type of mechanism. *Nature.* 191:144–148.
2. Rich, P. R. 2003. The molecular machinery of Keilin's respiratory chain. *Biochem. Soc. Trans.* 31:1095–1105.
3. Pitkanen, S., and B. H. Robinson. 1996. Mitochondrial complex I deficiency leads to increased production of superoxide radicals and induction of superoxide dismutase. *J. Clin. Invest.* 98:345–351.
4. Valsecchi, F., C. Monge, …, P. H. Willems. 2012. Metabolic consequences of NDUFS4 gene deletion in immortalized mouse embryonic fibroblasts. *Biochim. Biophys. Acta.* 1817:1925–1936.
5. Wu, S. B., and Y. H. Wei. 2012. AMPK-mediated increase of glycolysis as an adaptive response to oxidative stress in human cells: implication of the cell survival in mitochondrial diseases. *Biochim. Biophys. Acta.* 1822:233–247.
6. Huppertz, C., B. M. Fischer, …, B. B. Kahn. 2001. Uncoupling protein 3 (UCP3) stimulates glucose uptake in muscle cells through a phosphoinositide 3-kinase-dependent mechanism. *J. Biol. Chem.* 276:12520–12529.
7. Saleem, A., A. Safdar, …, M. A. Tarnopolsky. 2015. Polymerase gamma mutator mice rely on increased glycolytic flux for energy production. *Mitochondrion.* 21:19–26.
8. Suhane, S., H. Kanzaki, …, V. K. Ramanujan. 2013. Mitochondrial NDUFS3 regulates the ROS-mediated onset of metabolic switch in transformed cells. *Biol. Open.* 2:295–305.
9. Barnes, K., J. C. Ingram, …, S. A. Baldwin. 2002. Activation of GLUT1 by metabolic and osmotic stress: potential involvement of AMP-activated protein kinase (AMPK). *J. Cell Sci.* 115:2433–2442.
10. Shetty, M., J. N. Loeb, …, F. Ismail-Beigi. 1993. Rapid activation of GLUT-1 glucose transporter following inhibition of oxidative phosphorylation in clone 9 cells. *J. Biol. Chem.* 268:17225–17232.
11. Shi, Y., H. Liu, …, C. Y. Jung. 1995. Modulation of GLUT1 intrinsic activity in clone 9 cells by inhibition of oxidative phosphorylation. *J. Biol. Chem.* 270:21772–21778.
12. Jing, M., V. K. Cheruvu, and F. Ismail-Beigi. 2008. Stimulation of glucose transport in response to activation of distinct AMPK signaling pathways. *Am. J. Physiol. Cell Physiol.* 295:C1071–C1082.
13. Hamrahian, A. H., J. Z. Zhang, …, F. Ismail-Beigi. 1999. Activation of Glut1 glucose transporter in response to inhibition of oxidative phosphorylation. *Arch. Biochem. Biophys.* 368:375–379.
14. Gambhir, S. S. 2002. Molecular imaging of cancer with positron emission tomography. *Nat. Rev. Cancer.* 2:683–693.
15. Young, C. D., A. S. Lewis, …, S. M. Anderson. 2011. Modulation of glucose transporter 1 (GLUT1) expression levels alters mouse mammary tumor cell growth in vitro and in vivo. *PLoS One.* 6:e23205.
16. Patergnani, S., F. Baldassari, …, P. Pinton. 2014. Methods to monitor and compare mitochondrial and glycolytic ATP production. *Methods Enzymol.* 542:313–332.

17. Haran, M., and A. Gross. 2014. Balancing glycolysis and mitochondrial OXPHOS: lessons from the hematopoietic system and exercising muscles. *Mitochondrion.* 19 Pt A:3–7.
18. Drozdowicz-Tomsia, K., A. G. Anwer, …, E. M. Goldys. 2014. Multiphoton fluorescence lifetime imaging microscopy reveals free-to-bound NADH ratio changes associated with metabolic inhibition. *J. Biomed. Opt.* 19:086016.
19. Dott, W., P. Mistry, …, K. E. Herbert. 2014. Modulation of mitochondrial bioenergetics in a skeletal muscle cell line model of mitochondrial toxicity. *Redox Biol.* 2:224–233.
20. Jose, C., N. Bellance, and R. Rossignol. 2011. Choosing between glycolysis and oxidative phosphorylation: a tumor's dilemma? *Biochim. Biophys. Acta.* 1807:552–561.
21. Lowe, A. G., and A. R. Walmsley. 1986. The kinetics of glucose transport in human red blood cells. *Biochim. Biophys. Acta.* 857:146–154.
22. Fehr, M., H. Takanaga, …, W. B. Frommer. 2005. Evidence for high-capacity bidirectional glucose transport across the endoplasmic reticulum membrane by genetically encoded fluorescence resonance energy transfer nanosensors. *Mol. Cell. Biol.* 25:11102–11112.
23. Barros, L. F., C. X. Bittner, …, O. H. Porras. 2007. A quantitative overview of glucose dynamics in the gliovascular unit. *Glia.* 55:1222–1237.
24. Wu, F., F. Yang, …, D. A. Beard. 2007. Computer modeling of mitochondrial tricarboxylic acid cycle, oxidative phosphorylation, metabolite transport, and electrophysiology. *J. Biol. Chem.* 282:24525–24537.
25. van Eunen, K., S. Rossell, …, B. M. Bakker. 2011. Quantitative analysis of flux regulation through hierarchical regulation analysis. *Methods Enzymol.* 500:571–595.
26. Marín-Hernández, A., J. C. Gallardo-Pérez, …, E. Saavedra. 2011. Modeling cancer glycolysis. *Biochim. Biophys. Acta.* 1807:755–767.
27. Alam, M. T., G. R. Manjeri, …, W. J. Koopman. 2015. Skeletal muscle mitochondria of *NDUFS4-/-* mice display normal maximal pyruvate oxidation and ATP production. *Biochim. Biophys. Acta.* 1847:526–533.
28. Takanaga, H., B. Chaudhuri, and W. B. Frommer. 2008. GLUT1 and GLUT9 as major contributors to glucose influx in HepG2 cells identified by a high sensitivity intramolecular FRET glucose sensor. *Biochim. Biophys. Acta.* 1778:1091–1099.
29. Takanaga, H., and W. B. Frommer. 2010. Facilitative plasma membrane transporters function during ER transit. *FASEB J.* 24:2849–2858.
30. Nooteboom, M., M. Forkink, …, W. J. H. Koopman. 2012. Live-cell quantification of mitochondrial functional parameters. *In* Visualization Techniques, *Vol. 70* Emilio Badoer, editor. Humana Press, NY, pp. 111–127.
31. Hutter, E., K. Renner, …, E. Gnaiger. 2004. Senescence-associated changes in respiration and oxidative phosphorylation in primary human fibroblasts. *Biochem. J.* 380:919–928.
32. Gnaiger, E. 2001. Bioenergetics at low oxygen: dependence of respiration and phosphorylation on oxygen and adenosine diphosphate supply. *Respir. Physiol.* 128:277–297.
33. Fehr, M., S. Lalonde, …, W. B. Frommer. 2003. In vivo imaging of the dynamics of glucose uptake in the cytosol of COS-7 cells by fluorescent nanosensors. *J. Biol. Chem.* 278:19127–19133.
34. John, S. A., M. Ottolia, …, B. Ribalet. 2008. Dynamic modulation of intracellular glucose imaged in single cells using a FRET-based glucose nanosensor. *Pflugers Arch.* 456:307–322.
35. Bittner, C. X., A. Loaiza, …, L. F. Barros. 2010. High resolution measurement of the glycolytic rate. *Front. Neuroenergetics.* 2:2.
36. Augustin, R. 2010. The protein family of glucose transport facilitators: It's not only about glucose after all. *IUBMB Life.* 62:315–333.
37. Carruthers, A., J. DeZutter, …, S. U. Devaskar. 2009. Will the original glucose transporter isoform please stand up! *Am. J. Physiol. Endocrinol. Metab.* 297:E836–E848.
38. Devés, R., and R. M. Krupka. 1978. Cytochalasin B and the kinetics of inhibition of biological transport: a case of asymmetric binding to the glucose carrier. *Biochim. Biophys. Acta.* 510:339–348.
39. Ulanovskaya, O. A., J. Cui, …, S. A. Kozmin. 2011. A pairwise chemical genetic screen identifies new inhibitors of glucose transport. *Chem. Biol.* 18:222–230.
40. Cloherty, E. K., K. B. Levine, and A. Carruthers. 2001. The red blood cell glucose transporter presents multiple, nucleotide-sensitive sugar exit sites. *Biochemistry.* 40:15549–15561.
41. Bertram, R., and M. Pernarowski. 1998. Glucose diffusion in pancreatic islets of Langerhans. *Biophys. J.* 74:1722–1731.
42. Deichmann, U., S. Schuster, …, A. Cornish-Bowden. 2014. Commemorating the 1913 Michaelis-Menten paper Die Kinetik der Invertinwirkung: three perspectives. *FEBS J.* 281:435–463.
43. Wilson, J. E. 2003. Isozymes of mammalian hexokinase: structure, subcellular localization and metabolic function. *J. Exp. Biol.* 206:2049–2057.
44. Cloherty, E. K., D. L. Diamond, …, A. Carruthers. 1996. Regulation of GLUT1-mediated sugar transport by an antiport/uniport switch mechanism. *Biochemistry.* 35:13231–13239.
45. Carruthers, A. 1990. Facilitated diffusion of glucose. *Physiol. Rev.* 70:1135–1176.
46. Liu, Q., J. C. Vera, …, D. W. Golde. 2001. The predicted ATP-binding domains in the hexose transporter GLUT1 critically affect transporter activity. *Biochemistry.* 40:7874–7881.
47. Rossignol, R., T. Letellier, …, J. P. Mazat. 2000. Tissue variation in the control of oxidative phosphorylation: implication for mitochondrial diseases. *Biochem. J.* 347:45–53.
48. Slomka, N., and A. Gefen. 2011. Cell-to-cell variability in deformations across compressed myoblasts. *J. Biomech. Eng.* 133:081007–081012.
49. Peeters, E. A., C. V. Bouten, …, F. P. Baaijens. 2004. Anisotropic, three-dimensional deformation of single attached cells under compression. *Ann. Biomed. Eng.* 32:1443–1452.
50. De Rasmo, D., G. Gattoni, …, A. Signorile. 2011. The β-adrenoceptor agonist isoproterenol promotes the activity of respiratory chain complex I and lowers cellular reactive oxygen species in fibroblasts and heart myoblasts. *Eur. J. Pharmacol.* 652:15–22.
51. Bermejo, C., F. Haerizadeh, …, W. B. Frommer. 2010. Dynamic analysis of cytosolic glucose and ATP levels in yeast using optical sensors. *Biochem. J.* 432:399–406.
52. Moussa, R., A. Baierl, …, M. Pohl. 2014. An evaluation of genetically encoded FRET-based biosensors for quantitative metabolite analyses in vivo. *J. Biotechnol.* 191:250–259.
53. Filippin, L., P. J. Magalhães, …, T. Pozzan. 2003. Stable interactions between mitochondria and endoplasmic reticulum allow rapid accumulation of calcium in a subpopulation of mitochondria. *J. Biol. Chem.* 278:39224–39234.
54. Kletzien, R. F., and J. F. Perdue. 1973. The inhibition of sugar transport in chick embryo fibroblasts by cytochalasin B. Evidence for a membrane-specific effect. *J. Biol. Chem.* 248:711–719.
55. Purich, D. L., and H. J. Fromm. 1971. The kinetics and regulation of rat brain hexokinase. *J. Biol. Chem.* 246:3456–3463.
56. Zou, C., Y. Wang, and Z. Shen. 2005. 2-NBDG as a fluorescent indicator for direct glucose uptake measurement. *J. Biochem. Biophys. Methods.* 64:207–215.
57. Jung, D. W., H. H. Ha, …, D. R. Williams. 2011. Novel use of fluorescent glucose analogues to identify a new class of triazine-based insulin mimetics possessing useful secondary effects. *Mol. Biosyst.* 7:346–358.
58. Barros, L. F., C. X. Bittner, …, M. Alvarez. 2009. Kinetic validation of 6-NBDG as a probe for the glucose transporter GLUT1 in astrocytes. *J. Neurochem.* 109 (*Suppl 1*):94–100.
59. Naftalin, R. J. 2008. Alternating carrier models of asymmetric glucose transport violate the energy conservation laws. *Biophys. J.* 95:4300–4314.
60. Bonder, E. M., and M. S. Mooseker. 1986. Cytochalasin B slows but does not prevent monomer addition at the barbed end of the actin filament. *J. Cell Biol.* 102:282–288.

61. Jing, M., and F. Ismail-Beigi. 2007. Critical role of 5′-AMP-activated protein kinase in the stimulation of glucose transport in response to inhibition of oxidative phosphorylation. *Am. J. Physiol. Cell Physiol.* 292:C477–C487.

62. Behrooz, A., and F. Ismail-Beigi. 1997. Dual control of glut1 glucose transporter gene expression by hypoxia and by inhibition of oxidative phosphorylation. *J. Biol. Chem.* 272:5555–5562.

63. Gunnink, S. M., S. A. Kerk, …, L. L. Louters. 2014. Alkaline pH activates the transport activity of GLUT1 in L929 fibroblast cells. *Biochimie.* 99:189–194.

64. Blodgett, D. M., J. K. De Zutter, …, A. Carruthers. 2007. Structural basis of GLUT1 inhibition by cytoplasmic ATP. *J. Gen. Physiol.* 130:157–168.

65. Levine, K. B., E. K. Cloherty, …, A. Carruthers. 2002. Molecular determinants of sugar transport regulation by ATP. *Biochemistry.* 41:12629–12638.

66. Reference deleted in proof.

67. Wu, N., B. Zheng, …, L. C. Cantley. 2013. AMPK-dependent degradation of TXNIP upon energy stress leads to enhanced glucose uptake via GLUT1. *Mol. Cell.* 49:1167–1175.

68. Hebert, D. N., and A. Carruthers. 1992. Glucose transporter oligomeric structure determines transporter function. Reversible redox-dependent interconversions of tetrameric and dimeric GLUT1. *J. Biol. Chem.* 267:23829–23838.

69. Zottola, R. J., E. K. Cloherty, …, A. Carruthers. 1995. Glucose transporter function is controlled by transporter oligomeric structure. A single, intramolecular disulfide promotes GLUT1 tetramerization. *Biochemistry.* 34:9734–9747.

70. De Zutter, J. K., K. B. Levine, …, A. Carruthers. 2013. Sequence determinants of GLUT1 oligomerization: analysis by homology-scanning mutagenesis. *J. Biol. Chem.* 288:20734–20744.

71. Kuipers, D. P., J. P. Scripture, …, L. L. Louters. 2013. Differential regulation of GLUT1 activity in human corneal limbal epithelial cells and fibroblasts. *Biochimie.* 95:258–263.

72. Wilson, J. E. 1995. Hexokinases. *Rev. Physiol. Biochem. Pharmacol.* 126:65–198.

73. Meglasson, M. D., and F. M. Matschinsky. 1983. Discrimination of glucose anomers by glucokinase from liver and transplantable insulinoma. *J. Biol. Chem.* 258:6705–6708.

74. Otaegui, P. J., M. Ontiveros, …, F. Bosch. 2002. Glucose-regulated glucose uptake by transplanted muscle cells expressing glucokinase counteracts diabetic hyperglycemia. *Hum. Gene Ther.* 13:2125–2133.

75. Bakker, B. M., M. C. Walsh, …, H. V. Westerhoff. 1999. Contribution of glucose transport to the control of the glycolytic flux in *Trypanosoma brucei*. *Proc. Natl. Acad. Sci. USA.* 96:10098–10103.

76. Mookerjee, S. A., R. L. Goncalves, …, M. D. Brand. 2015. The contributions of respiration and glycolysis to extracellular acid production. *Biochim. Biophys. Acta.* 1847:171–181.

77. Distelmaier, F., F. Valsecchi, …, W. J. Koopman. 2015. Mitochondrial dysfunction in primary human fibroblasts triggers an adaptive cell survival program that requires AMPK-α. *Biochim. Biophys. Acta.* 1852:529–540.